frontiers in Astronomy and Space Sciences

ORIGINAL RESEARCH
published: 27 October 2021
doi: 10.3389/fspas.2021.746459

Mesoscale Features in the Global Geospace Response to the March 12, 2012 Storm

Mayowa Adewuyi[1], *Amy M. Keesee*[1,2]*, *Yukitoshi Nishimura*[3], *Christine Gabrielse*[4] and *Roxanne M. Katus*[5]

[1]*Department of Physics and Astronomy, University of New Hampshire, Durham, NH, United States,* [2]*Space Science Center, Institute for Earth, Oceans, and Space, University of New Hampshire, Durham, NH, United States,* [3]*Department of Electrical and Computer Engineering and Center for Space Physics, Boston University, Boston, MA, United States,* [4]*The Aerospace Corporation, El Segundo, CA, United States,* [5]*Department of Mathematics and Statistics, Eastern Michigan University, Ypsilanti, MI, United States*

The geospace response to coronal mass ejections includes phenomena across many regions, from reconnection at the dayside and magnetotail, through the inner magnetosphere, to the ionosphere, and even to the ground. Phenomena occurring in each region are often connected to each other through the magnetic field, but that field undergoes dynamic changes during storms and substorms. Improving our understanding of the geospace response to storms requires a global picture that enables us to observe all the regions simultaneously with both spatial and temporal resolution. Using the Energetic Neutral Atom (ENA) imager on the Two Wide-Angle Imaging Neutral-Atom Spectrometers (TWINS) mission, a temperature map can be calculated to provide a global view of the magnetotail. These maps are combined with *in situ* measurements at geosynchronous orbit from GOES 13 and 15, auroral images from all sky imagers (ASIs), and ground magnetometer measurements to examine the global geospace response of a coronal mass ejection (CME) driven event on March 12th, 2012. Mesoscale features in the magnetotail are observed throughout the interval, including prior to the storm commencement and during the main phase, which has implications for the dominant processes that lead to pressure buildup in the inner magnetosphere. Auroral enhancements that can be associated with these magnetotail features through magnetosphere-ionosphere coupling are observed to appear only after global reconfigurations of the magnetic field.

Keywords: geomagnetic storm, substorm, magnetotail, particle injections, mesoscale phenomena

OPEN ACCESS

Edited by:
Hermann Lühr,
Helmholtz Centre Potsdam, Germany

Reviewed by:
Evgeny Panov,
Austrian Academy of Sciences, Austria
Huishan Fu,
Beihang University, China

Correspondence:
Amy M. Keesee
amy.keesee@unh.edu

Specialty section:
This article was submitted to Space Physics, a section of the journal Frontiers in Astronomy and Space Sciences

Received: *23 July 2021*
Accepted: *13 October 2021*
Published: *27 October 2021*

Citation:
Adewuyi M, Keesee AM, Nishimura Y, Gabrielse C and Katus RM (2021) Mesoscale Features in the Global Geospace Response to the March 12, 2012 Storm. Front. Astron. Space Sci. 8:746459. doi: 10.3389/fspas.2021.746459

INTRODUCTION

During geomagnetic storms and substorms, magnetic reconnection in Earth's magnetotail can accelerate ions and electrons both Earthward and tailward (e.g. Hoshino et al., 2001; Drake et al., 2006; Fu et al., 2019). Bursty bulk flows (BBFs) and dipolarization fronts (DFs) are Earthward traveling features that can result from this reconnection-driven acceleration (Baumjohann et al., 1990, 1999; Angelopoulos et al., 1992, 1994; Nakamura et al., 2002; Runov et al., 2009; Fu et al., 2013). BBFs are continuous segments of magnetotail flow enhancement (~10 min), punctuated by ~1 min long intense flow and electric field bursts ($V > 400$ km/s, $VB_z > 2$ mV/m). DFs are a sharp increase in

Bz with thickness on the order of the ion inertial length. Statistical analysis by Fu et al. (2012) showed that these DFs have a peak occurrence at a radial distance of approximately 15 R_E, and occurrence decreases rapidly inside r ~ 10 R_E. Using simulation results, Merkin et al. (2019a) demonstrated the correlation between substorm onset and abrupt increase in DF counts, noting this increase as a characteristic of the substorm onset. These reconnection fast flows and related DFs are narrow--on the order of a few R_E wide (Sergeev et al., 1996; Nakamura et al., 2004). These phenomena in the tail are associated with particle injections-observed as rapid increases in energetic particle fluxes-in the near tail and inner magnetosphere (Birn et al., 1997).

There is debate about whether the buildup of the ring current pressure is caused by these mesoscale phenomena or by broad earthward convection resulting from a southward *z*-component of the interplanetary magnetic field (IMF). Menz et al. (2017) used Van Allen Probes measurements and drift trajectory modeling to show that adiabatic convection was sufficient to explain the ring current pressure buildup for two storms. However, the fast flows and DFs have been shown to carry >60% of the measured earthward transport of mass, energy and magnetic flux using a statistical study of *in situ* measurements (Angelopoulos et al., 1994). Because of their narrow nature, it is extremely difficult to put BBFs into the global context for a specific event with only single-point *in situ* satellite measurements that will easily miss the signature. Modeling of several idealized storms demonstrated a similar contribution from mesoscale phenomena (~61% for intense storms) and that these injections were required to recreate observed ring current enhancements in the simulations (Yang et al., 2015; 2016). A global view of the near-Earth region is needed to provide context to localized measurements and validate simulations.

The plasma sheet where these mesoscale phenomena occur magnetically maps to the ionosphere. Many studies have shown the connection between phenomena in the magnetotail and auroral enhancements (e.g. Elphinstone et al., 1995; Henderson et al., 1998; Sergeev et al., 2000, 2004) and we discuss a few highlights here. Motoba et al. (2012) used conjugate auroral observations in the northern and southern hemispheres to demonstrate that auroral beads (wave-like structures) appearing in the initial brightening arc just before substorm onset have a source in the magnetotail with scales on the order of the 1–10 keV proton gyroradius. Spanswick et al. (2017) used THEMIS and FAST satellite-based measurements and ground-based proton aurora images to statistically determine that most of the proton aurora originates from 6–10 R_E. Lyons et al. (2012) demonstrated a connection between dipolarization fronts in the plasma sheet and aurora streamers and discussed the implications for substorm onset. Ge et al. (2012) found connections between dipolarization fronts and proton aurora observations and used magnetohydrodynamics (MHD)-based simulations to determine that proton aurora enhancements were caused by ion reflection at the front. Nishimura et al. (2014) connected transient flow bursts in the magnetotail and ring current injections measured by THEMIS with proton aurora observed by all sky imagers. Nakamura et al. (2001) used Geotail measurements and Polar UVI images to show that auroral streamers correspond to field aligned currents on the dusk side of earthward flow bursts. Auroral streamers have been used to demonstrate that BBFs are seen to enter and terminate within the transition region from stretched to dipolar-like field lines in the tail (Kauristie et al., 2003). It is in this transition region that Gabrielse et al. (2019) showed minutes-long ion injections with flux enhancements that lasted approximately for the duration of the earthward flow. Both the flow and the ion injection were quenched when the global dipolarization (and associated substorm auroral expansion seen in the THEMIS ASIs) expanded over the observing satellites. Donovan et al. (2013) notes that more observations of this transition region are needed to better understand the physics of this region, particularly to understand substorm onset.

All of these studies supplemented and informed the ionosphere observations with localized *in situ* measurements in the magnetotail that provide limited spatial coverage. While comparison to simulations can provide more context to the global response of the system, global measurements are needed to provide validation. Energetic neutral atom (ENA) imaging can provide this needed global view of the magnetosphere. Ion temperature maps can be calculated using ENA measurements (Scime et al., 2002; Keesee et al., 2008) and used to look for heated ions associated with phenomena in the magnetotail. This technique requires active intervals for sufficient ENA signal (McComas et al., 2002; Keesee et al., 2014). DFs are associated with a gradual increase in ion temperature ahead of the front (Runov et al., 2011) due to the acceleration and reflection of ions in the plasma sheet ahead of the front (Zhou et al., 2010). Ukhorskiy et al. (2018) found that this energization is higher than would be expected from an adiabatic process. Ion temperatures tend to remain elevated for a longer time interval than the short time scales during which the flow bursts occur (Angelopoulos et al., 1992). The dipolarization of the magnetic field associated with substorms and injections also results in energization of ions through a process similar to betatron acceleration (Birn et al., 1997).

Keesee et al. (2014) observed regions of energized ions in the magnetotail during the Galaxy-15 substorm using TWINS energetic neutral atom (ENA) data to calculate ion temperature maps. These energized regions are observed to move Earthward and are deflected azimuthally near geosynchronous orbit. Keesee et al. (2020) compared TWINS ion temperature maps, MMS data, and MHD simulations for an interval during August 3, 2016. Multiple regions of enhanced ion temperatures are observed during this period across the tail in the TWINS maps. One of these regions occurred on the dusk side of the tail near the location of the MMS satellites. This region increased from ~5 to >10 keV as calculated from TWINS data. During this interval MMS4 observed increased ion energies, Earthward flow bursts (Vx), increased ion temperatures, and a dipolarization of Bz. The MHD simulations of this interval also had increased ion temperatures and flows associated with substorm activity. However, the heating in the simulations was less than that observed in the data, demonstrating that global

ENA imaging is critical to validating models and improving our understanding of substorm dynamics.

In this study, we combine global ENA imaging with *in situ* measurements in the inner magnetosphere and auroral imaging to improve our understanding of mesoscale phenomena in the magnetotail and their connections to the inner magnetosphere and ionosphere.

DATA AND METHODOLOGY

TWINS Ion Temperature Maps

The Two Wide-angle Imaging Neutral atom Spectrometers (TWINS) mission (McComas et al., 2009) provides energetic neutral atom data from two satellites in high inclination Molniya orbits. Ion temperature maps are calculated by projecting ENA flux with energies of 1–36 keV along the line of sight to the equatorial plane and fitting to a Maxwellian distribution for parent ions (Scime et al., 2002; Keesee et al., 2008). The resulting mapped area is a combination of the instrument field of view and a modeled magnetosphere boundary using Shue et al. (1997). The map is a grid of 0.5×0.5 R_E bins that are populated by flux from a varying number of projected instrument pixels, resulting in a spatial resolution that decreases with increasing distance from Earth (Keesee et al., 2014, 2011). A database of temperature maps at 10-min cadence during storms is available at CDAWeb (Keesee et al., 2020) and the projection and temperature analysis codes are available in the UNH Scholar's Repository (Keesee et al., 2019). For this study, temperature maps were created using a ~3-min cadence.

In Situ Measurements

Inner magnetosphere measurements during the storm are available from the Time History of Events and Macroscale Interactions during Substorm (THEMIS) mission (Angelopoulos, 2008) and NOAA Geostationary Operational Environmental Satellite (GOES) 13 and 15. THEMIS consists of three identically-instrumented satellites with apogees of ~12 R_E. Ion flux measurements are provided by the electrostatic analyzer (ESA) (5 eV–25 keV ions) (McFadden et al., 2008) and the Solid State Telescope (SST) (30 to >700 keV ions) (Angelopoulos et al., 2008) and magnetic field measurements from the fluxgate magnetometer (FGM) (Auster et al., 2008). The GOES satellites include a Space Environment Monitor (SEM) instrument subsystem that obtains magnetometer, energetic particle, and soft X-ray data (Singer et al., 1996; Onsager et al., 1996).

Auroral Imagers

The THEMIS mission includes an array of 20 white light auroral imagers across Greenland, Canada, and Alaska (Harris et al., 2008; Mende et al., 2008). These All Sky Imagers (ASI) provide images with several km spatial resolution and 3 s temporal resolution. ASI images cannot be used to distinguish between electron and proton aurora, but conjugate observations from satellites such as THEMIS and GOES electron and proton fluxes can be used to identify proton aurora in the images (Nishimura et al., 2014).

Ground Magnetometers

Ground magnetic field perturbations are obtained from the SuperMAG database (Gjerloev, 2012). Data was obtained from 201 magnetometer stations. Station location is used to determine magnetic local time.

RESULTS

A CME-driven storm occurred on March 12, 2012 (Keesee and Scime, 2015) with a sudden storm commencement beginning at 9:16 UT and a minimum Sym-H index of -67 nT at 16:55 UT. The overall evolution of the storm is shown in **Figure 1**, including interplanetary magnetic field (IMF) z-component, AE index, solar wind pressure, Sym-H index, proton flux from GOES 13 and 15, average plasma sheet ion temperature from TWINS, and average ground magnetic field perturbations from SuperMag stations for mid (50–60) and high (> 60) latitudes. The overall trend in the temperature of the plasma sheet corresponds with the trends in the AE index and SuperMAG ground magnetic field perturbations, showing connections between the plasma sheet and the ionosphere. There are three separate peaks observed in these variables, one at the beginning of the storm, the second associated with a southward turning of the IMF Bz, and the third following a prolonged period of strong southward Bz.

A sudden storm commencement (SSC) can be observed around 9:15 UT (vertical line 1 in **Figure 1**), with a very strong (>50 nT) increase to the Sym-H index driven by the high solar wind pressure. We note that the increase in Sym-H (**Figure 1D**) appears prior to the increase in solar wind pressure (**Figure 1C**) which may be due to inaccurate propagation of the data measured at the Lagrangian L1 point to the bow shock. An increase in the proton flux was measured by *in situ* satellites shortly after the SSC, with GOES 13 observing the flux increase slightly before GOES 15. During this time interval, GOES 13 was located pre-dawn at approximately −5.5 R_E in Y and −3 R_E in X (GSM coordinates), while GOES 15 was located near midnight at approximately −0.1 R_E in Y and −5.8 R_E in X (see GOES and THEMIS orbital locations in the **Supplementary Material**). Both GOES satellites observed a simultaneous increase in flux across all energies for both protons and electrons (electrons not shown). THEMIS satellites located toward the dawn flank from GOES 13 observed similar flux increases (see **Supplementary Material**). This is typically interpreted as a signature of the plasma sheet's earthward boundary moving earthward of the satellite location by magnetosphere compression and global E x B convection. However, as we will describe in the Discussion, this could be a signature of dispersionless injection. The SSC was preceded by consistent southward IMF Bz for approximately 90 min. A northward turning of the IMF Bz can be seen around 9:45 UT (vertical line 2 in **Figure 1**), with the AE index also decreasing around the same time and the Sym-H index remaining near zero. A

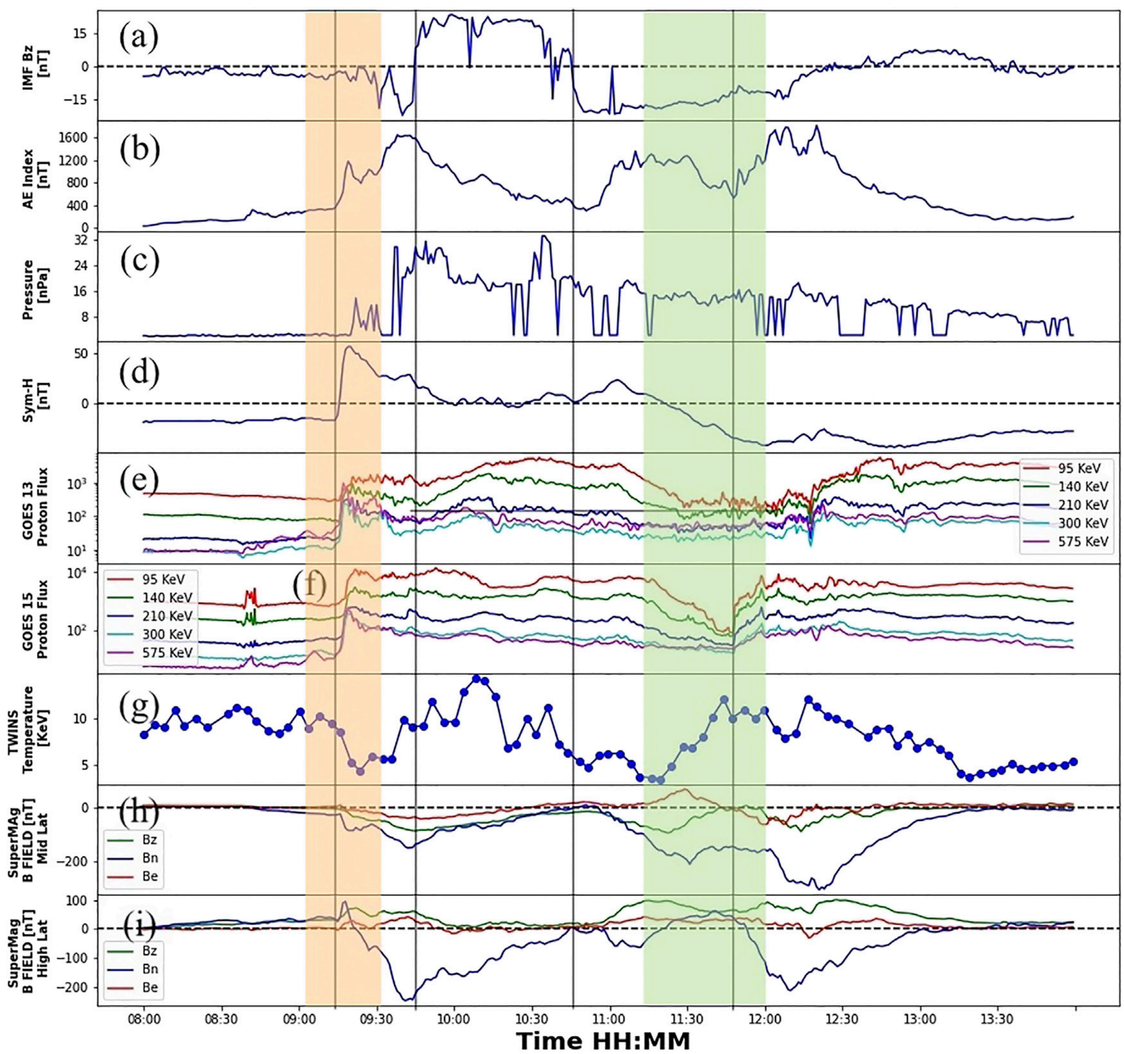

FIGURE 1 | (A) IMF Bz, **(B)** AE index, **(C)** solar wind pressure, and **(D)** Sym-H index from OMNIWeb, GOES **(E)** 13 and **(F)** 15 proton flux [p/cm2 s sr keV], **(G)** TWINS average plasma sheet ion temperature, SuperMAG ground magnetic field perturbations averaged for **(H)** mid and **(I)** high latitude stations for March 12, 2012, 8:00–14:00 UT. Vertical lines indicate times referenced in the text. The shaded regions correspond to intervals discussed in the text and highlighted in **Figures 2**, **3** (orange) and **Figures 4**, **5** (green).

decrease in the temperature of the plasma sheet occurred shortly afterwards at around 10:15 UT. Ground perturbations were observed at the SSC, with the averaged SuperMag magnetic field changing in response, especially in the local magnetic north component. The high latitude SuperMAG average was positive for about 4 min after the SSC, before a negative bay that peaked around 9:45 UT. The mid latitude stations experienced a less intense perturbation that peaked at the same time.

Figure 2 shows a sequence of ion temperature maps calculated from TWINS for 9:04–9:33 UT (orange highlighted interval in **Figure 1**). This series of temperature maps give a global observation of the plasma sheet during the interval surrounding the SSC. The average temperature shown in **Figure 1** is calculated from these maps by selecting the area from 5 to 20 R_E and magnetic local time (MLT) from 20:00 to 4:00. A movie of ion temperature maps for the entire storm interval is in the **Supplementary Material**. Regions of increased ion temperatures are observed prior to the SSC, likely due to the steady southward IMF Bz prior to the shock arrival driving tail reconnection and earthward flows (as evidenced by the AE index increasing to ~400 nT in **Figure 1B**). At the time of the SSC, the plasma sheet temperatures drop significantly across the entire field of view, as seen in **Figure 2D**. Regions of increased ion temperature begin appearing again in the 9:22–9:26 UT interval (**Figure 2F**) with the most intense region occurring in the dusk half of the magnetotail. These regions appear localized across the magnetotail and elongated along the tail and move towards the inner magnetosphere, indicative

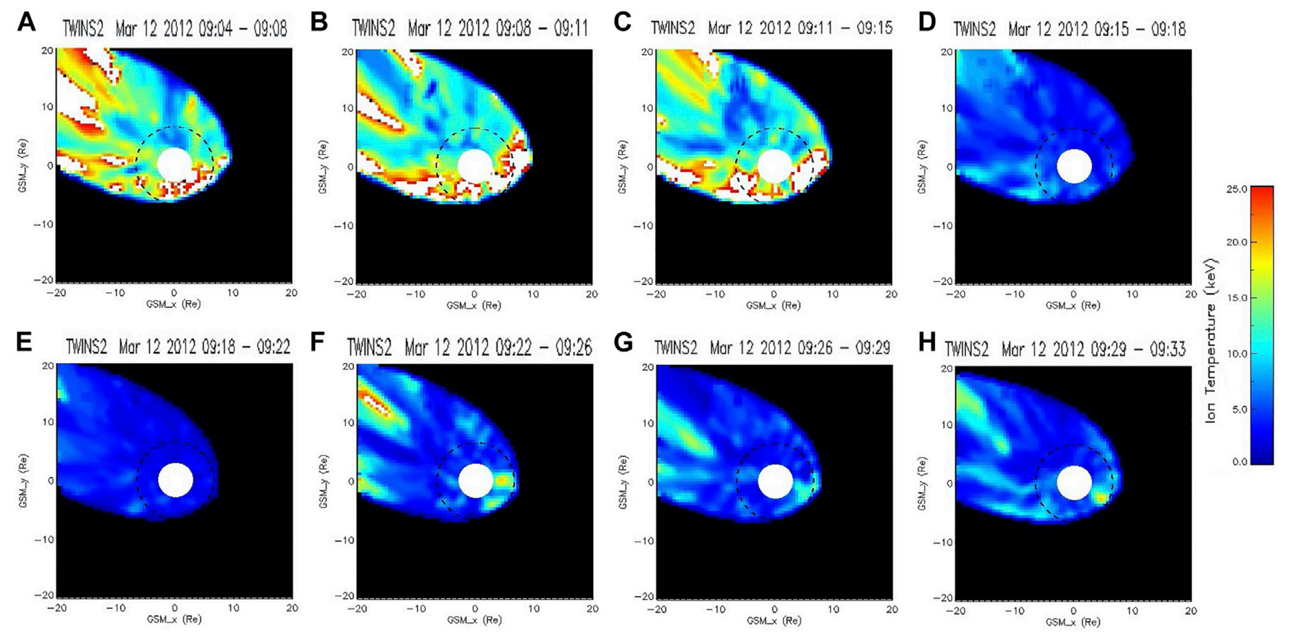

FIGURE 2 | Ion temperature maps of the GSM xy-plane calculated from TWINS measurements for 9:04–9:33 UT. The Sun is to the right, the white disc has a radius of 3 Re and is centered at Earth and the dashed line indicates geosynchronous orbit.

of narrow flow channels. Note, however, that because the temperature maps are ~3 min averages the flows do not necessarily exist across the entire length for the full interval.

The THEMIS All Sky Imagers can provide spatial and temporal evolution of ionospheric activity. The ASI movie is in the **Supplementary Material**. To compare locations of observations to TWINS measurements, the TS01 model was used to map THEMIS ASI images and the locations of the *in situ* spacecraft to the GSM equatorial plane. The magnetic field model is not necessarily accurate, particularly at outer L-shells. As such, we do not intend to make pixel-to-pixel comparisons, and instead compare overall morphology. A sequence of mapped ASI images and the associated globe projections for 9:05–9:30 UT are shown in **Figure 3**. Despite the continuous southward IMF Bz, the auroral activity is minimal (the moonlight is blocked and appears white) until after the SSC at 9:15 UT (**Figure 3C**) with initial brightening occurring in the region mapping to post-midnight. A poleward boundary intensification (PBI) is observed prior to SSC (**Figure 3B**). Streamers are identified in each interval after the SSC. At 9:25 UT (**Figure 3E**), brightening occurs in the pre-midnight region and extends to post-midnight. This brightening is identified as a streamer in the pre-midnight region of the ASI.

The IMF Bz turned southward around 10:45 UT (vertical line 3 in **Figure 1**) resulting in moderate increases in the AE index, plasma sheet temperatures, and ground magnetic field perturbations approximately 10–15 min later. As the Bz remained strongly southward, the plasma sheet ion temperature increased and dispersionless ion injections were observed at geosynchronous orbit. A strong response was seen in the SuperMAG data, and the AE and Sym-H indices peaked about 10 min after the injection observed at GOES 15.

A sequence of ion temperature maps calculated from TWINS from 11:13–11:56 UT (green highlighted interval in **Figure 1**) is shown in **Figure 4**. This series shows the plasma sheet during the interval of strong southward IMF Bz. Regions of increased ion temperatures are observed in the plasma sheet, primarily on the dawn (post-midnight) side of the tail. These regions appear to first reach geosynchronous orbit in the 11:20–11:24 UT interval (**Figure 4C**). As time continues, there are more regions and they increase in size across the tail. The flux dropout observed by GOES-15 (located post-midnight) at 11:20–11:47 UT corresponds to the substorm growth phase during the southward IMF, when the magnetic field stretched, resulting in the satellite moving away from the central plasma sheet (**Figure 1F**). A dispersionless injection is observed by GOES-15 at 11:47 UT (vertical line 4 in **Figure 1**). GOES-13 (located at dawn) observed a flux dropout similar to GOES-15 (**Figure 1E**). The magnetic field at this location didn't change much, so the flux variations don't seem to be due to magnetic field stretching. The lower energy ion fluxes dropped, while high energy ion fluxes didn't change much, which could be indicative of magnetopause shadowing.

The sequence of ASI projections for 11:15–12:00 UT is shown in **Figure 5**. Auroral activity is minimal until 11:45 UT (**Figure 5G**), after which the enhancements in the post-midnight imager expand tailward.

To understand the spatial correlation between signatures in the temperature maps and the ground observations, plots of magnetic perturbation as a function of MLT and UT are shown in **Figure 6** for low (0–50°), mid (50–60°), and high

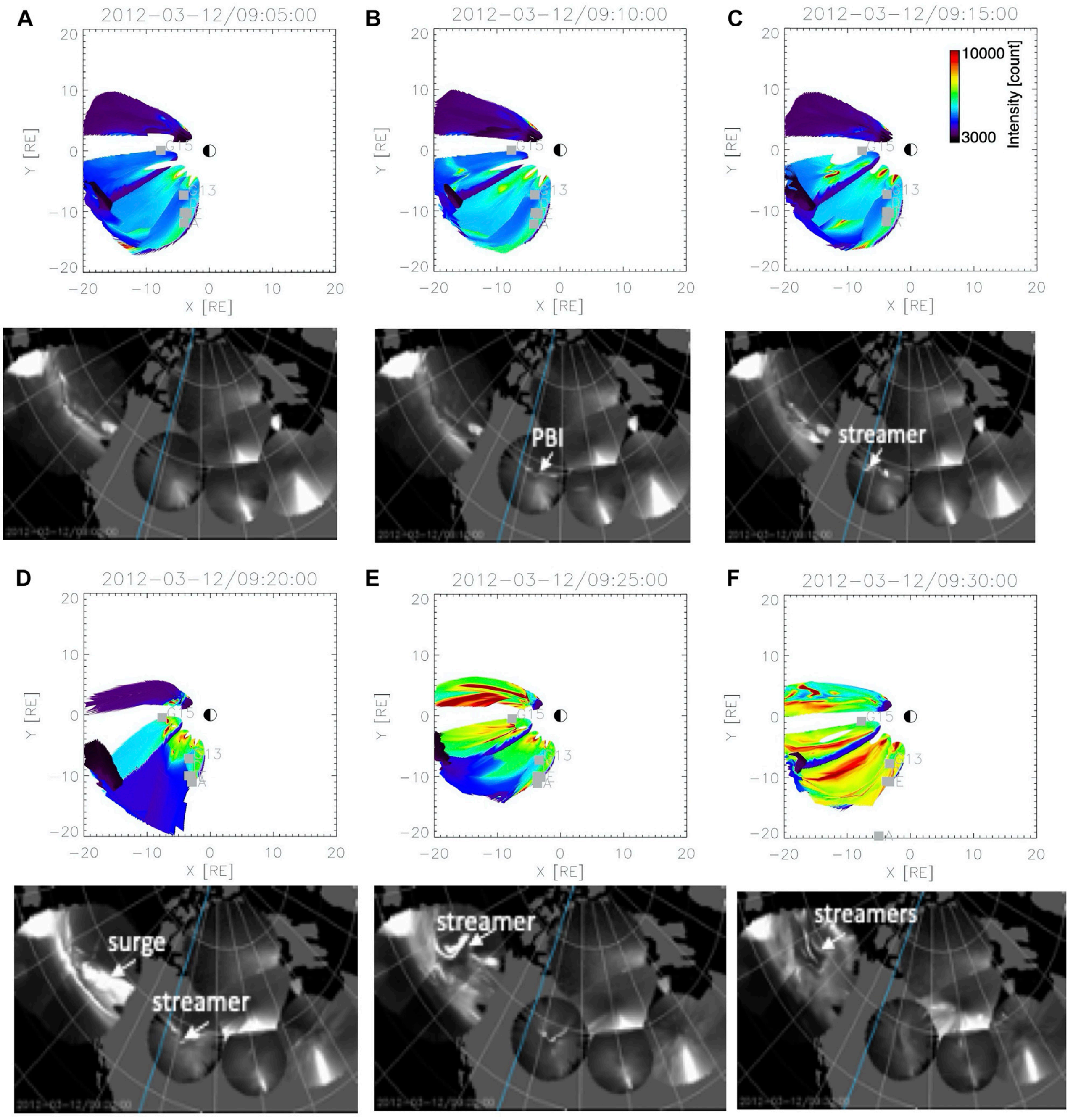

FIGURE 3 | THEMIS ASI auroral images mapped to the GSM equatorial plane using TS01 **(top)** and globe projections **(bottom)** for 9:05–9:30 UT. The colorbar in panel **(C)** applies to all panels. Symbols indicate the mapped location of the GOES 13 (G13), GOES 15 (G15), and THEMIS (A, D, E) satellites.

(60–90°) latitudes. Very weak perturbations in the magnetic field at low latitudes (**Figure 6A**) can be seen, with the strongest perturbation reaching about 400 nT in magnitude. The mid latitude stations (**Figure 6B**) observed some stronger perturbations, going as far up as 1600 nT. The location of the highest magnetic field perturbations was also confined within the 0–10 MLT (i.e., post-midnight). The high latitude stations (**Figure 6C**) observed the strongest perturbations, with some stations going up to 2000 nT in magnitude. The locations of the highest changes in the fields were broader in comparison to the mid latitude stations, going from about 18 to 10 MLT. Across all latitudes, three distinct temporal regions of increased perturbations can be seen, starting from the SSC at 9:15 UT, and then at 11:00 UT, with a final increase occurring shortly afterwards at approximately 12:00 UT. While the first

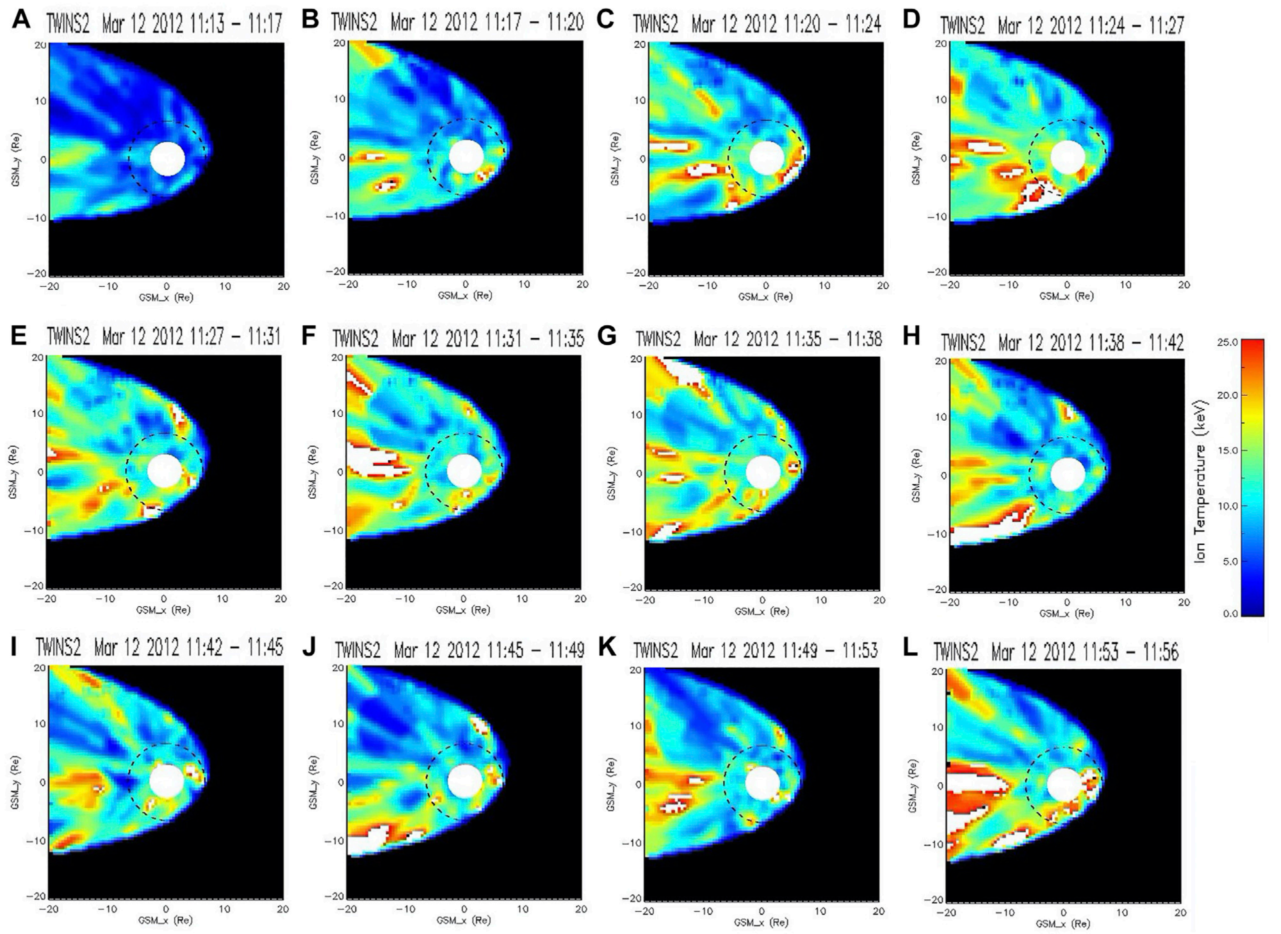

FIGURE 4 | Ion temperature maps of the GSM xy-plane calculated from TWINS measurements for 11:13–11:56. The Sun is to the right, the white disc has a radius of 3 Re and is centered at Earth and the dashed line indicates geosynchronous orbit.

two peaks appear to stay mostly stationary in MLT, the third peak appears to move toward noon over time.

DISCUSSION

Using a multi-perspective global view, we found that mesoscale phenomena played a significant role during this storm. As described above, the initial flux increase at the SSC is typically interpreted as a global phenomenon due to compression of the magnetosphere. However, there were multiple mesoscale features observed in the TWINS maps prior to the SSC that could have led to particle injections to the inner magnetosphere. The Sym-H response to the SSC was significantly stronger than typical storms, perhaps indicating that a combination of changes, including injection of particles, was occurring to the inner magnetosphere. A decrease in the ion temperature across the magnetosphere was also observed at the time of the SSC. It is unclear if this is a physical result or a reduction in ENA flux to the instrument due to global reconfiguration of the magnetic field. More studies using global imaging are needed to compare pre-storm plasma sheet conditions and the resulting inner magnetosphere SSC response.

While the southward turning of the IMF Bz at ~10:45 UT resulted in moderate activity, as observed by the ground observations and AE index, more significant activity was observed following prolonged southward Bz while the plasma sheet had the opportunity to heat up. The average plasma sheet temperature begins to decrease at the same time as the GOES 13 (located at dawn) flux begins to decrease (~11:10 UT in **Figure 1E–G**). Then, the temperature increase begins at the same time as the flux decrease at GOES 15 (located post-midnight) began (~11:20 in **Figure 1F,G**). An injection is observed at GOES 15 and the AE begins to increase to its highest value during the storm just after the plasma sheet reaches its peak temperature. This agrees with the findings by Forsyth et al. (2014) that plasma sheet ion temperatures during the substorm growth phase increase with solar wind driving and also correlate with substorm size. The multiple mesoscale features observed by TWINS during the growth phase agrees qualitatively with simulations

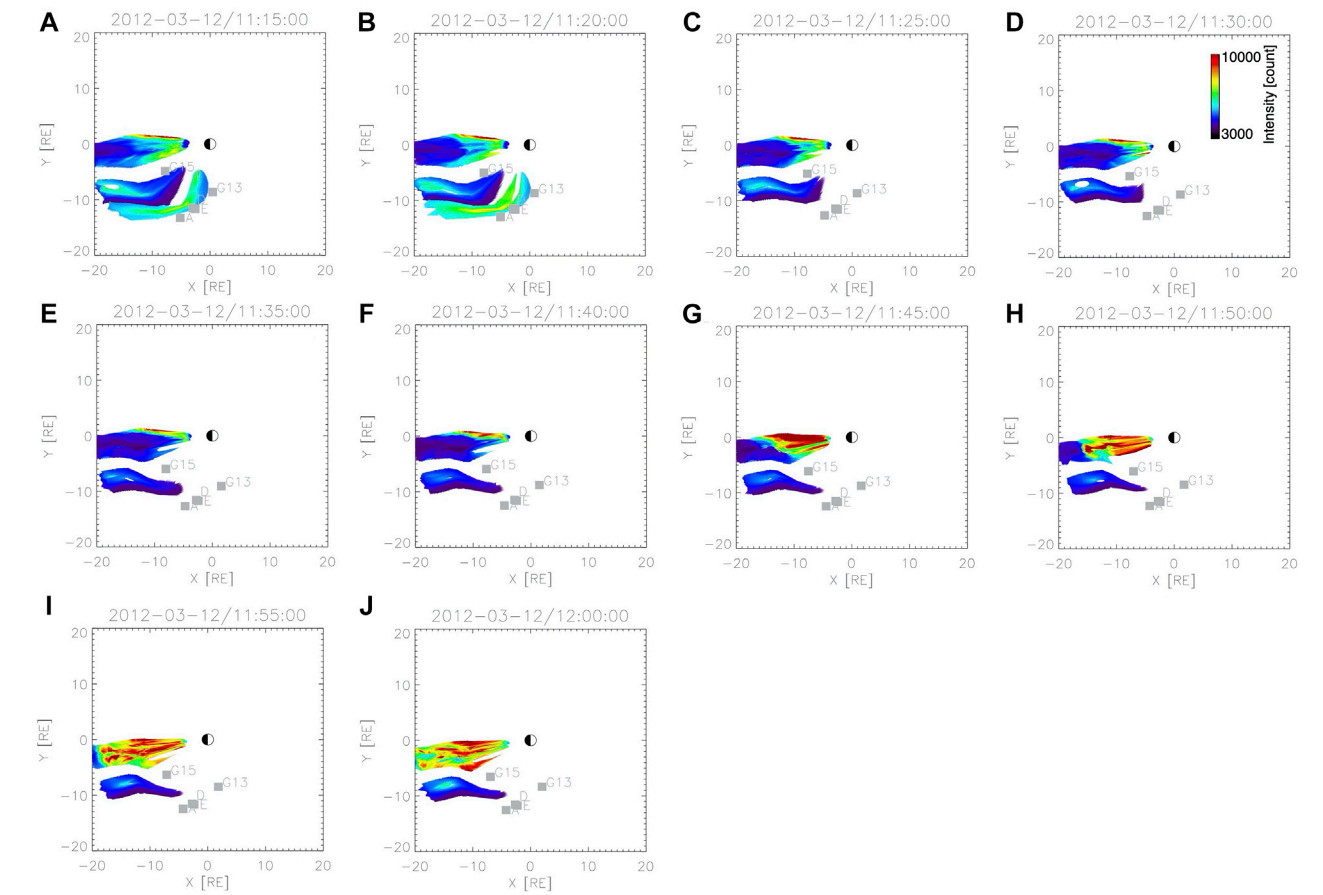

FIGURE 5 | THEMIS ASI auroral images mapped to the GSM equatorial plane using TS01 for 9:15–12:00 UT. The colorbar in panel **(D)** applies to all panels. Symbols indicate the mapped location of the GOES 13 (G13), GOES 15 (G15), and THEMIS (A, D, E) satellites.

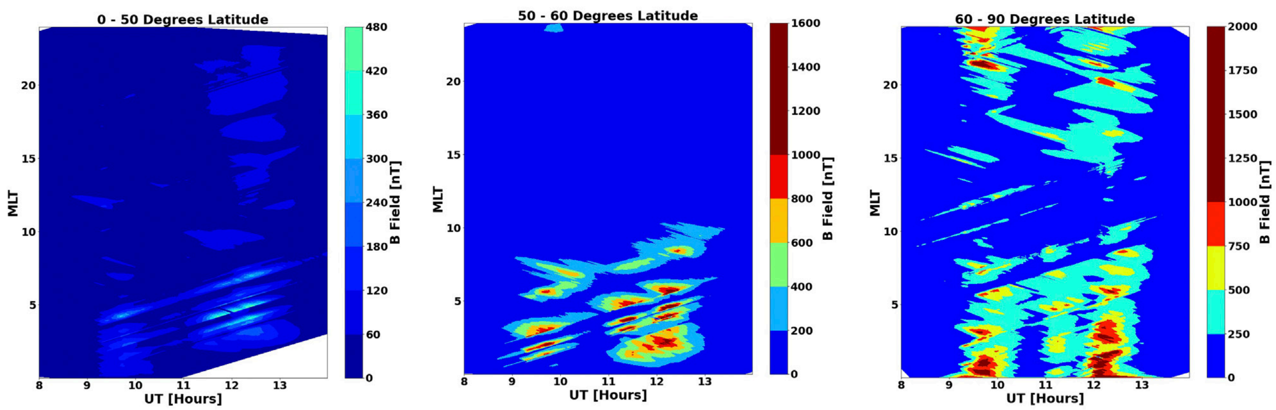

FIGURE 6 | Ground magnetic field north component perturbations as a function of location (MLT) and time (UT) for **(A)** low, **(B)** mid, and **(C)** high latitudes using SuperMAG data. Note that each plot is on the same color scale, but the colorbar indicates the range of values within the plot.

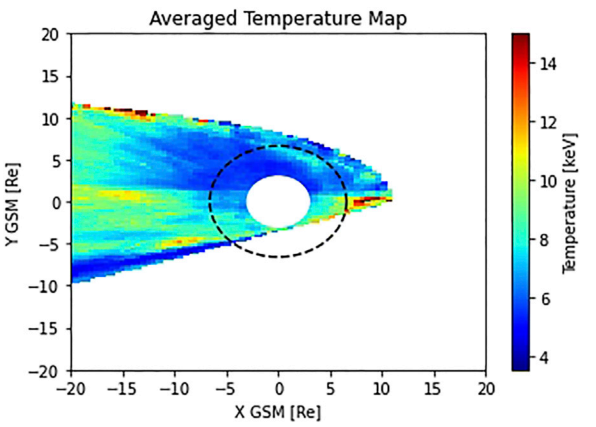

FIGURE 7 | Average temperature map for the entire storm interval, 8:00–13:30 UT. The white disk has a radius of 3 Re centered on Earth, while the dashed circle indicates geosynchronous orbit. The color bar limit goes up only to 15 keV, as opposed to 25 keV from the previous temperature maps.

by Merkin et al. (2019b), and direct comparisons of such simulations with TWINS temperature maps during the same interval would be useful for future studies.

We note that the increased temperatures occur predominantly on the dawn (post-midnight) side of the magnetotail during the ~11–12 UT interval (**Figure 4**), which makes this storm unique in that it contrasts with the majority of fast flows and injections that have been observed on the dusk (pre-midnight) side (McPherron et al., 2011; Liu et al., 2013; Walsh et al., 2014; Gabrielse et al., 2017). To emphasize this, an ion temperature map averaged over the entire storm is shown in **Figure 7**. While this average over 5.5 h demonstrates some variations due to instrumental effects (the TWINS ENA instrument consists of two sensor heads), recall that primarily dusk-side regions are observed early in the storm (**Figure 2**). Additionally, the localization of the enhancements in the ASI projections and mid-latitude ground perturbations to the post-midnight sector corresponds to the predominance of increased plasma sheet temperatures to the same region.

As noted in the description of **Figure 6**, the third overall increase in ground magnetic perturbations (starting just before 12:00 UT) showed movement in MLT toward noon over time. This is indicative of particles flowing around Earth, and can also be observed in the ion temperature maps (see movie in **Supplementary Material**). This is in contrast to the first two increases, and only occurred after the heating of the plasma sheet, demonstrating the role that plasma sheet dynamics have in particle motion in the inner magnetosphere.

The regions of increased ion temperatures observed in the plasma sheet were observed to first reach geosynchronous orbit in the 11:20–11:24 UT interval (**Figure 4C**). However, increases in flux are not observed at GOES until 11:47 UT, though as indicated GOES is probably outside of the central plasma sheet due to magnetic field stretching. Thus, the global imaging from TWINS enables us to see that particles are likely entering the inner magnetosphere earlier than is observable by the *in situ* measurements. However, the ASI enhancements are also observed at about the same time as the GOES flux increase. At the time when GOES observes the flux increase, both TWINS and ASI observed enhancements in the post-midnight region (**Figures 4J**, **5G**). GOES 15 mapped to a location −6.7 Re in X, and −6.6 Re in Y, just on the edge of the region of hot ion plasma seen in the temperature map. A flux increase in the GOES 15 data can be seen across all energy levels. Since the regions of heated ions are observed in the plasma sheet prior to the injection at GOES but no significant features were observed in the aurora until after the injection, the reconfiguration of the magnetic field caused by the substorm must have provided a stronger connection between the plasma sheet and ionosphere after than time. A similar reconfiguration appears to occur at the beginning of the storm since the auroral brightening occurs after SSC despite the observation of heated ions in the plasma sheet prior to it.

CONCLUSION

We have analyzed the global response of the geospace system, from the plasma sheet in the magnetotail to the ground, for the storm on March 12, 2012. By taking advantage of global imaging techniques, spatial and temporal signatures of the plasma sheet's response to the CME driven event was observed. Observations of the plasma sheet before the SSC show signatures of flow channels coming in from the magnetotail, indicating the importance of mesoscale injections to the inner magnetosphere at SSC. This may have combined with global convection to result in a strong Sym-H response at SSC. The temperature maps during the storm main phase showed a flow channel bias towards the post-midnight sector. This bias towards this sector was also seen in the ground observations, with regions within 18 MLT to 10 MLT experiencing stronger magnetic perturbations. Comparison with auroral images demonstrates a change in magnetosphere-ionosphere coupling upon both the commencement of the storm and the onset of a substorm.

DATA AVAILABILITY STATEMENT

Publicly available datasets were analyzed in this study. This data can be found here: The TWINS and THEMIS datasets analyzed for this study can be found at CDAWeb (https://cdaweb.gsfc.nasa.gov/index.html/). GOES datasets can be found at NOAA (https://www.ngdc.noaa.gov/stp/satellite/goes/dataaccess.html). Ground magnetometer data is available at the SuperMAG site (https://supermag.jhuapl.edu). Solar wind, IMF, and geomagnetic indices can be found at OMNIWeb (https://omniweb.gsfc.nasa.gov).

AUTHOR CONTRIBUTIONS

MA and AK conducted the primary analysis and writing of the manuscript. YN and RK contributed to data analysis and figure creation. YN and CG contributed to data interpretation. YN, CG, and RK reviewed the draft and provided input.

FUNDING

Funding provided by NASA Awards 80NSSC19K0755, 80NSSC20K0701, 80NSSC18K0657, 80NSSC20K0604, 80NSSC20K0725 and NSF Awards 2109543, AGS-1602862, AGS-1907698, and AFOSR Grant FA9559-16-1-0364.

ACKNOWLEDGMENTS

The authors would like to thank Victor Pinto for helpful discussions.

SUPPLEMENTARY MATERIAL

The Supplementary Material for this article can be found online at: https://www.frontiersin.org/articles/10.3389/fspas.2021.746459/full#supplementary-material

REFERENCES

Angelopoulos, V., Baumjohann, W., Kennel, C. F., Coroniti, F. V., Kivelson, M. G., Pellat, R., et al. (1992). Bursty Bulk Flows in the Inner Central Plasma Sheet. *J. Geophys. Res.* 97 (A4), 4027–4039. doi:10.1029/91ja02701

Angelopoulos, V., Kennel, C. F., Coroniti, F. V., Pellat, R., Kivelson, M. G., Walker, R. J., et al. (1994). Statistical characteristics of bursty bulk flow events. *J. Geophys. Res.* 99 (A11), 21257. doi:10.1029/94JA01263

Angelopoulos, V., Sibeck, D., Carlson, C. W., McFadden, J. P., Larson, D., Lin, R. P., et al. (2008). First results from the THEMIS mission. *Space Sci. Rev.* 141 (1–4), 453–476. doi:10.1007/s11214-008-9378-4

Angelopoulos, V. (2008). The THEMIS Mission. *Space Sci. Rev.* 141 (1–4), 5–34. doi:10.1007/s11214-008-9336-1

Auster, H. U., Glassmeier, K. H., Magnes, W., Aydogar, O., Baumjohann, W., Constantinescu, D., et al. (2008). The THEMIS fluxgate magnetometer. *Space Sci. Rev.* 141 (1–4), 235–264. doi:10.1007/s11214-008-9365-9

Baumjohann, W., Hesse, M., Kokubun, S., Mukai, T., and Nagai, T. (1999). Substorm dipolarization and recovery Baumjohann et did a superposed epoch observed fast earthward flows in the plasma sheet sis of substorm phase signatures in the How- boundary layer starting at the beginning of the recovery ever. *since the the AMPTE*/104, 995–1000. doi:10.1029/1999ja900282

Baumjohann, W., Paschmann, G., and Lühr, H. (1990). Characteristics of high-speed ion flows in the plasma sheet. *J. Geophys. Res.* 95 (A4), 3801–3809. doi:10.1029/ja095ia04p03801

Birn, J., Thomsen, M. F., Borovsky, J. E., Reeves, G. D., McComas, D. J., Belian, R. D., et al. (1997). Substorm ion injections: Geosynchronous observations and test particle orbits in three-dimensional dynamic MHD fields. *J. Geophys. Res.* 102 (A2), 2325–2341. doi:10.1029/96JA03032

Donovan, E., Spanswick, E., Liang, J., Grant, J., Jackel, B., and Greffen, M. (2013). Magnetospheric Dynamics and the Proton Aurora. *Earth and Other Planets*, 365–378. doi:10.1029/2012GM001241

Drake, J. F., Swisdak, M., Phan, T. D., Cassak, P. a., Shay, M. a., Lepri, S. T., et al. (2009). Ion heating resulting from pickup in magnetic reconnection exhausts. *J. Geophys. Res.* 114 (A5), a–n. doi:10.1029/2008JA013701

Elphinstone, R. D., Hearn, D. J., Cogger, L. L., Murphree, J. S., Singer, H., Sergeev, V., et al. (1995). Observations in the vicinity of substorm onset: Implications for the substorm process. *J. Geophys. Res.* 100 (A5), 7937. doi:10.1029/94ja02938

Forsyth, C., Watt, C. E. J., Rae, I. J., Fazakerley, a. N., Kalmoni, N. M. E., Freeman, M. P., et al. (2014). Increases in plasma sheet temperature with solar wind driving during substorm growth phases. *Geophys. Res. Lett.* doi:10.1002/2014GL062400

Fu, H. S., Cao, J. B., Khotyaintsev, Y. V., Sitnov, M. I., Runov, A., Fu, S. Y., et al. (2013). Dipolarization fronts as a consequence of transient reconnection: *In situ* evidence. *Geophys. Res. Lett.* 40 (23), 6023–6027. doi:10.1002/2013GL058620

Fu, H. S., Khotyaintsev, Y. V., Vaivads, A., André, M., and Huang, S. Y. (2012). Occurrence rate of earthward-propagating dipolarization fronts. *Geophys. Res. Lett.* 39, L10101. doi:10.1029/2012GL051784

Fu, H. S., Xu, Y., Vaivads, A., and Khotyaintsev, Y. V. (2019). Super-efficient Electron Acceleration by an Isolated Magnetic Reconnection. *ApJ* 870 (2), L22. doi:10.3847/2041-8213/aafa75

Gabrielse, C., Runov, A., Angelopoulos, V., Spanswick, E., and Turner, D. L. (2017). Premidnight preponderance of dispersionless ion and electron injections. *Dawn-Dusk Asymmetries Planet. Plasma Environments*, 171–185. doi:10.1002/9781119216346.ch13

Gabrielse, C., Spanswick, E., Artemyev, A., Nishimura, Y., Runov, A., Lyons, L., et al. (2019). Utilizing the Heliophysics/Geospace System Observatory to Understand Particle Injections: Their Scale Sizes and Propagation Directions. *J. Geophys. Res. Space Phys.* 124, 5584–5609. doi:10.1029/2018ja025588

Ge, Y. S., Zhou, X.-Z., Liang, J., Raeder, J., Gilson, M. L., Donovan, E., et al. (2012). Dipolarization fronts and associated auroral activities: 1. Conjugate observations and perspectives from global MHD simulations. *J. Geophys. Res.* 117 (10), a–n. doi:10.1029/2012JA017676

Gjerloev, J. W. (2012). The SuperMAG data processing technique. *J. Geophys. Res.* 117 (9), A09213. doi:10.1029/2012JA017683

Harris, S. E., Mende, S. B., Angelopoulos, V., Rachelson, W., Donovan, E., Jackel, B., et al. (2008). THEMIS ground based observatory system design. *Space Sci. Rev.* 141 (1–4), 213–233. doi:10.1007/s11214-007-9294-z

Henderson, M. G., Reeves, G. D., and Murphree, J. S. (1998). Are north-south aligned auroral structures an ionospheric manifestation of bursty bulk flows. *Geophys. Res. Lett.* 25 (19), 3737–3740. doi:10.1029/98GL02692

Hoshino, M., Mukai, T., Terasawa, T., and Shinohara, I. (2001). Suprathermal electron acceleration in magnetic reconnection. *J. Geophys. Res.* 106 (A11), 25979–25997. doi:10.1029/2001ja900052

Kauristie, K., Sergeev, V. A., Amm, O., Kubyshkina, M. V., Jussila, J., Donovan, E., et al. (2003). Bursty bulk flow intrusion to the inner plasma sheet as inferred from auroral observations. *J. Geophys. Res.* 108 (A1), 1–9. doi:10.1029/2002JA009371

Keesee, A. M., Buzulukova, N., Goldstein, J., Mccomas, D. J., Scime, E. E., Spence, H., et al. (2011). Remote observations of ion temperatures in the quiet time magnetosphere. *Geophys. Res. Lett.* 38, L03104. doi:10.1029/2010GL045987

Keesee, A. M., Buzulukova, N., Mouikis, C., and Scime, E. E. (2021). Mesoscale Structures in Earth's Magnetotail Observed Using Energetic Neutral Atom Imaging. *Geophys. Res. Lett.* 48, e2020GL091467. doi:10.1029/2020gl091467

Keesee, A. M., Chen, M. W., Scime, E. E., and Lui, A. T. Y. (2014). Regions of ion energization observed during the Galaxy-15 substorm with TWINS. *J. Geophys. Res. Space Phys.* 119, 8274–8287. doi:10.1002/2014JA020466

Keesee, A. M., Katus, R. M., Floyd, M., and Scime, E. E. (2020). Database of Storm Time Equatorial Ion Temperatures in Earth's Magnetosphere Calculated from Energetic Neutral Atom Data. *J. Geophys. Res. Space Phys.* 125, e2020JA028266. doi:10.1029/2020JA028266

Keesee, A. M., and Scime, E. E. (2015). Database of ion temperature maps during geomagnetic storms. *Earth Space Sci.* 2, 39–46. doi:10.1002/2014EA000061

Keesee, Amy. M., Scime, E., and Moldwin, M. B. (2008). Remote measurements of ion temperatures in the terrestrial magnetotail. *J. Geophys. Res. Space Phys.* 113, A00A03. doi:10.1029/2008JA013130

Keesee, A., Scime, E., Zaniewski, A., and Katus, R. (2019). 2D Ion Temperature Maps from TWINS ENA data: IDL scripts. *UNH Scholars' Repository*. doi:10.34051/c/2019.1

Liu, J., Angelopoulos, V., Runov, A., and Zhou, X.-Z. (2013). On the current sheets surrounding dipolarizing flux bundles in the magnetotail: The case for wedgelets. *J. Geophys. Res. Space Phys.* 118 (5), 2000–2020. doi:10.1002/jgra.50092

Lyons, L. R., Nishimura, Y., Xing, X., Runov, A., Angelopoulos, V., Donovan, E., et al. (2012). Coupling of dipolarization front flow bursts to substorm expansion phase phenomena within the magnetosphere and ionosphere. *J. Geophys. Res.* 117, A02212. doi:10.1029/2011JA017265

McComas, D. J., Allegrini, F., Baldonado, J., Blake, B., Brandt, P. C., Burch, J., et al. (2009). The Two Wide-angle Imaging Neutral-atom Spectrometers (TWINS) NASA Mission-of-Opportunity. *Space Sci. Rev.* 142 (1–4), 157–231. doi:10.1007/s11214-008-9467-4

McComas, D. J., Valek, P., Burch, J. L., Pollock, C. J., Skoug, R. M., and Thomsen, M. F. (2002). Filling and emptying of the plasma sheet: Remote observations with 1-70 keV energetic neutral atoms. *Geophys. Res. Lett.* 29 (22), 2079. doi:10.1029/2002GL016153

McFadden, J. P., Carlson, C. W., Larson, D., Ludlam, M., Abiad, R., Elliott, B., et al. (2008). The THEMIS ESA Plasma Instrument and In-flight Calibration. *Space Sci. Rev.* 141 (1–4), 277–302. doi:10.1007/s11214-008-9440-2

McPherron, R. L., Hsu, T.-S., Kissinger, J., Chu, X., and Angelopoulos, V. (2011). Characteristics of plasma flows at the inner edge of the plasma sheet. *J. Geophys. Res.* 116 (4), 1–19. doi:10.1029/2010JA015923

Mende, S. B., Harris, S. E., Frey, H. U., Angelopoulos, V., Russell, C. T., Donovan, E., et al. (2008). The THEMIS array of ground-based observatories for the study of auroral substorms. *Space Sci. Rev.* 141 (1–4), 357–387. doi:10.1007/s11214-008-9380-x

Menz, A. M., Kistler, L. M., Mouikis, C. G., Spence, H. E., Skoug, R. M., Funsten, H. O., et al. (2017). The role of convection in the buildup of the ring current pressure during the 17 March 2013 storm. *J. Geophys. Res. Space Phys.* 122 (122), 475–492. doi:10.1002/2016JA023358

Merkin, V. G., Panov, E. V., Sorathia, K. A., and Ukhorskiy, A. Y. (2019a). Contribution of Bursty Bulk Flows to the Global Dipolarization of the Magnetotail during an Isolated Substorm. *J. Geophys. Res. Space Phys.* 124, 8647–8668. doi:10.1029/2019JA026872

Merkin, V. G., Panov, E. V., Sorathia, K. A., and Ukhorskiy, A. Y. (2019b). Contribution of Bursty Bulk Flows to the Global Dipolarization of the Magnetotail during an Isolated Substorm. *J. Geophys. Res. Space Phys.* 124 (11), 8647–8668. doi:10.1029/2019JA026872

Motoba, T., Hosokawa, K., Kadokura, A., and Sato, N. (2012). Magnetic conjugacy of northern and southern auroral beads. *Geophys. Res. Lett.* 39, L08108. doi:10.1029/2012GL051599

Nakamura, M. S., Matsumoto, H., and Fujimoto, M. (2002). Interchange instability at the leading part of reconnection jets. *Geophys. Res. Lett.* 29 (8). doi:10.1029/2001GL013780

Nakamura, R., Baumjohann, W., Mouikis, C., Kistler, L. M., Runov, A., Volwerk, M., et al. (2004). Spatial scale of high-speed flows in the plasma sheet observed by Cluster. *Geophys. Res. Lett.* 31, L09804. doi:10.1029/2004GL019558

Nakamura, R., Baumjohann, W., Schödel, R., Brittnacher, M., Sergeev, V. A., Kubyshkina, M., et al. (2001). Earthward flow bursts, auroral streamers, and small expansions. *J. Geophys. Res.* 106 (A6), 10791–10802. doi:10.1029/2000ja000306

Nishimura, Y., Bortnik, J., Li, W., Lyons, L. R., Donovan, E. F., Angelopoulos, V., et al. (2014). Evolution of nightside subauroral proton aurora caused by transient plasma sheet flows. *J. Geophys. Res. Space Phys.* 119 (7), 5295–5304. doi:10.1002/2014JA020029

Onsager, T., Grubb, R., Kunches, J., Matheson, L., Speich, D., Zwickl, R. W., Sauer, H., et al. (1996). "Operational Uses of the GOES Energetic Particle Detectors," in SPIE's 1996 International Symposium on Optical Science, Engineering, and Instrumentation, Denver, CO, October 18, 1996 (Denver, CO: SPIE) 2812. doi:10.1117/12.254075

Runov, A., Angelopoulos, V., Sitnov, M. I., Sergeev, V. a., Bonnell, J., McFadden, J. P., et al. (2009). THEMIS observations of an earthward-propagating dipolarization front. *Geophys. Res. Lett.* 36 (14), L14106. doi:10.1029/2009GL038980

Runov, A., Angelopoulos, V., Zhou, X.-Z., Zhang, X.-J., Li, S., Plaschke, F., et al. (2011). A THEMIS multicase study of dipolarization fronts in the magnetotail plasma sheet. *J. Geophys. Res.* 116 (A5), A05216. doi:10.1029/2010JA016316

Scime, E. E., Keesee, A. M., Jahn, J.-M., Kline, J. L., Pollock, C. J., and Thomsen, M. (2002). Remote ion temperature measurements of Earth's magnetosphere: Medium energy neutral atom (MENA) images. *Geophys. Res. Lett.* 29 (10), 1438. doi:10.1029/2001gl013994

Sergeev, V. A., Angelopoulos, V., Gosling, J. T., Cattell, C. A., and Russell, C. T. (1996). Detection of localized, plasma-depleted flux tubes or bubbles in the midtail plasma sheet. *J. Geophys. Res.* 101 (A5), 10817–10826. doi:10.1029/96ja00460

Sergeev, V. A., Liou, K., Newell, P. T., Ohtani, S.-I., Hairston, M. R., and Rich, F. (2004). Auroral streamers: characteristics of associated precipitation,convection and field-aligned currents. *Ann. Geophys.* 22, 537–548. doi:10.5194/angeo-22-537-2004

Sergeev, V. A., Sauvaud, J.-A., Popescu, D., Kovrazhkin, R. A., Liou, K., Newell, P. T., et al. (2000). Multiple-spacecraft observation of a narrow transient plasma jet in the Earth's plasma sheet. *Geophys. Res. Lett.* 27 (6), 851–854. doi:10.1029/1999GL010729

Shue, J.-H., Chao, J. K., Fu, H. C., Russell, C. T., Song, P., Khurana, K. K., et al. (1997). A new functional form to study the solar wind control of the magnetopause size and shape. *J. Geophys. Res.* 102 (A5), 9497–9511. doi:10.1029/97JA00196

Singer, H., Matheson, L., Grubb, R., Newman, A., and Bouwer, D. (1996). "Monitoring Space Weather with the GOES Magnetometers," in SPIE's 1996 International Symposium on Optical Science, Engineering, and Instrumentation, Denver, CO, October 18, 1996 (Denver, CO: SPIE) 2812, 299–308. doi:10.1117/12.254077

Spanswick, E., Donovan, E., Kepko, L., and Angelopoulos, V. (2017). The Magnetospheric Source Region of the Bright Proton Aurora. *Geophys. Res. Lett.* 44 (2010), 094. doi:10.1002/2017GL074956

Ukhorskiy, A. Y., Sorathia, K. A., Merkin, V. G., Sitnov, M. I., Mitchell, D. G., and Gkioulidou, M. (2018). Ion Trapping and Acceleration at Dipolarization Fronts: High-Resolution MHD and Test-Particle Simulations. *J. Geophys. Res. Space Phys.* 123 (7), 5580–5589. doi:10.1029/2018JA025370

Walsh, A. P., Haaland, S., Forsyth, C., Keesee, a. M., Kissinger, J., Li, K., et al. (2014). Dawn-dusk asymmetries in the coupled solar wind-magnetosphere-ionosphere system: a review. *Ann. Geophys.* 32 (7), 705–737. doi:10.5194/angeo-32-705-2014

Yang, J., Toffoletto, F. R., and Wolf, R. A. (2016). Comparison study of ring current simulations with and without bubble injections. *J. Geophys. Res. Space Phys.* 121, 374–379. doi:10.1002/2015JA021567

Yang, J., Toffoletto, F. R., Wolf, R. A., and Sazykin, S. (2015). On the contribution of plasma sheet bubbles to the storm time ring current. *J. Geophys. Res. Space Phys.* 120, 7416–7432. doi:10.1002/2016JA023362

Zhou, X.-Z., Angelopoulos, V., Sergeev, V. a., and Runov, a. (2010). Accelerated ions ahead of earthward propagating dipolarization fronts. *J. Geophys. Res.* 115 (May), a–n. doi:10.1029/2010JA015481

Conflict of Interest: CG was employed by The Aerospace Corporation.

The remaining authors declare that the research was conducted in the absence of any commercial or financial relationships that could be construed as a potential conflict of interest.